Nanoporous Gold by Alloy Corrosion: Method-Structure-Property Relationships

M. Graf,[a,z] B. Roschning,[a] and J. Weissmüller[a,b]

[a] *Institute of Materials Physics and Technology, Hamburg University of Technology, Hamburg, Germany*
[b] *Institute of Materials Research, Materials, Mechanics, Helmholtz-Zentrum Geesthacht, Geesthacht, Germany*

Nanoporous gold (NPG) made by selective corrosion, or dealloying, serves as a model system for the investigation of electrochemical and mechanical properties of nanomaterials. While various dealloying protocols are in use, it is typically assumed that the structural characteristics are identical and independent of the preparation technique. Yet, reported properties such as strength, Young's modulus, or catalytic behavior can vary widely. Here, we compare the microstructure and the mechanical behavior of NPG structures prepared by three different synthesis protocols reported in the literature. We find that corrosion rates, the content of residual sacrificial metal, the average ligament size and the densification by shrinkage strongly depend on the synthesis protocol and show the consequences on the mechanical properties. We finally deduce different correlations between microstructure and composition for different dealloying routes.

Manuscript submitted January 26, 2017; revised manuscript received February 20, 2017. Published March 4, 2017.

Nanoporous gold (NPG) made by dealloying is widely studied as advanced catalyst,[1–3] as material for sensing,[4] actuation[5,6] and energy storage,[7,8] as high surface-area electrode[9] or as electrically switchable microfluidics component.[10] Dealloying is the removal of the less noble element from a solid solution or intermetallic compound (e.g. Au-Ag,[11–13] Au-Cu[13,14] or Au-Al[15,16]) by selective corrosion. NPG exhibits an open-cell nanoscale network structure with a well-defined characteristic size of the metal phase, the so-called ligaments. These can be scaled ranging from as small as 5 nm up to 1 μm[17–21] so that NPG established as a model system for the investigation of nanoscale materials behavior.

Studies of the catalytic or mechanical behavior of NPG by different authors do not report consistent observations in all instances. The role of the residual sacrificial metal content as an origin for the remarkable catalytic activity (e.g. for CO oxidation) is under discussion.[22–25] As another instance, reports on the mechanical strength and stiffness of nominally comparable structures disagree by up to one order of magnitude.[26,27] Therefore it is significant to note that a number of different dealloying protocols are applied within these studies. Conceivably, diverging observations on the material's behavior may be related to the impact of these protocols on the microstructure. Here, we explore this issue by comparing the microstructures of NPG made by three common preparation routes.

The elementary steps of dealloying are the removal of atoms of the less noble element from the parent phase and the redistribution of the nobler element atoms on the crystal lattice by surface diffusion.[21] This creates a network structure, typically with sizes between 5 and 20 nm.[28,29] When assuming complete removal of the less noble element from a parent alloy (e.g. Ag_xAu_{1-x} which is composed of similarly sized atoms), the solid volume fraction, φ, of the porous structure will ideally agree with the atom fraction of the more noble element in the master alloy. Yet, the shrinkage during dealloying may reduce the external sample dimensions, thereby increasing φ.[29] Structural coarsening begins during dealloying[28] and its rate is affected e.g. by the composition of the electrolyte,[30] additional alloy elements[31,32] or the temperature.[33] These observations emphasize that details of the dealloying process may have a substantial effect on the microstructure of the nanoporous material.

Table I lists several synthesis protocols for NPG; these are often implicitly expected to result in similar structures. As the object of our study we selected three of the most common dealloying routes, namely potentiostatic dealloying under high polarization potential in $HClO_4$ (route A), potentiostatic dealloying under low polarization potential in HNO_3 (route B) and free corrosion under open-circuit conditions in HNO_3 (route C). The rather high electrolyte concentration in route B (which is minimum to result in a serious corrosion effect, but close to the free corrosion conditions of route C) besides the low polarization potential suggests that a considerable cathodic reaction could consume part of the true anodic current and the measured current does not reflect the extent of actual dealloying.

The results reveal systematic differences in the corrosion rate, the microstructural evolution over time and the mechanical behavior that may be of substantial impact for the comparison of NPG made by different techniques.

Experimental

The fabrication of $Ag_{75}Au_{25}$ alloy foils started out with arc-melting the pure metals (Au 99.995%, Ag 99.99%, both Chempur) and subsequent annealing at 925°C under vacuum atmosphere for 5 days. The alloy ingots were cold-rolled in at least three successive rolling-annealing (300°C, 10 min) cycles to achieve a foil thickness $l_0 = 130 - 160$ μm. Laser-cutting produced circular disks of 5 mm in diameter. Their outer surface area was 0.41 cm^2, as used for calculating the current density, j. Final cleaning used acetone, ethanol and water under ultrasonic agitation. l_0 of each specimen was determined as an average over three readings with a photoelectric length gauge (Heidenhain MT30B) that was calibrated to the thickness as measured by scanning electron microscopy (SEM).

Electrochemical dealloying was performed at room temperature in a three-electrode setup (electrolyte volume: 200 ml) with a glass capillary for the reference electrode (RE), a counter electrode (CE) separated from the main electrolyte compartment by a glass frit, the alloy as working electrode (WE) and controlled by a potentiostat (Metrohm Autolab PGStat10). Prior to dealloying, cyclic voltammetry (CV) scans (at 100 mV/s) were carried out to estimate a dealloying potential, E_d. Potentiostatic dealloying was performed within two different routes:

Route A followed Parida et al.[29] We used 1 M $HClO_4$ (Merck, 70–72%) as electrolyte, a polished and coiled Ag wire as CE and Ag/AgCl RE (Metrohm) with 3 M KCl internal electrolyte, along with $E_d^A = +1050$ mV (vs. Ag/AgCl) for dealloying durations, $t = 6 - 24$ h. Additional subsequent potential steps were applied in order to increase the amount of removed Ag (see Fig. 2D for the assignment to each step's duration); this resulted in total dealloying durations of 32, 40 or 50 h.

[z] E-mail: matthias.graf@tuhh.de

Table I. Overview over dealloying processes for Ag_xAu_{1-x}. Abbreviations: L_B = ligament diameter in bulk nanoporous gold; RE = reference electrode; MSE = Mercury/Mercury sulfate electrode; NHE = Normal hydrogen electrode; conc. = concentrated; *E* const = potentiostatic conditions; *I* const = amperostatic conditions; *E* ramp = controlled potential increase over time; *U* const = two-electrode setup with constant voltage; *U* pulsed = two-electrode setup with square-wave potential pulses over time. The methods under study in this work are highlighted in bold.

Process	Electrolyte	Electrochemistry		L_B	Reference
		Program	Duration	*nm*	
A	**1 M $HClO_4$**	***E* const, 890–1090 mV (vs. Ag/AgCl)**	-	**4-20**	**Parida**[29]
Variant of A	1 M $HClO_4$	*E* const, 1090 mV (vs. Ag/AgCl)	< 10 µA	21	Jin[34]
	0.7 M $HClO_4$	*I* const, 1–10 mA/cm²	100 s	30	Okman[35]
		E ramp 0 to 1300 mV (vs. Ag/AgCl)	30 s	10-15	Senior[12]
		E const, 1200 mV (vs. Ag/AgCl)	-	10-15	
	0.77 M $HClO_4$	*E* const, 920 - 1100 mV (vs. MSE)	30 s – 3 h	30	
B	**5.2 M HNO_3**	***E* const, 60 mV (vs. Pt)**	-	**50**	**Wittstock**[19,24]
Variant of B	5.2 M HNO_3	*U* const 570–870 mV	70 + 10 h	14	Sun[36]
	8 M HNO_3	*U* pulsed	20 min	8	Chen[37]
	conc. HNO_3	*U* const. 700 mV	10 min	15	Fujita[38]
C	**7.25 M HNO_3** (50°C)	**No polarization potential**	**48 h**	**47**	**Rouya**[39]
Variant of C	conc. HNO_3	No polarization potential	48 h	55	Qian[33]
D	0.1 M $AgNO_3$	*E* const. 1300–2000 mV (NHE)	-	5	Snyder[40]

The strategy of *route B* followed Wittstock et al.,[19] with 5 M HNO_3 (Merck, 65%) as electrolyte, Pt foils as CE and RE (offset vs. Ag/AgCl before dealloying: +270 mV) and $E_d^B = +60$ mV (vs. Pt) for $t = 6 - 24$ h.

Route C implemented dealloying under free corrosion conditions according to Rouya et al.[39] Here, the alloy sample was immersed in 7.25 M HNO_3 (Merck, 65%) at 60°C for $t = 6 - 24$ h.

After dealloying, the samples were rinsed in deionized water and dried in air for SEM and energy-dispersive X-ray spectroscopy (EDX) characterization. These were done within one day after dealloying, using a Leo Gemini 1530 microscope. Ligament sizes were derived from SEM micrographs at 250000X magnification by averaging a number of 20 diameters yielding also the values for standard deviations. EDX spectra were recorded from 20 × 30 µm areas of fracture surfaces to determine the residual Ag content in the bulk, x_{Ag}. Relative thickness changes were calculated by comparing the current NPG sample thickness, l with the initial thickness, l_0.

In order to prevent curling and cracking during drying, samples for nanoindentation were removed from the dealloying cell, washed with water and ethanol and dried under vacuum. The hardness was determined via instrumented indentation testing, measuring load and displacement using a MTS XP Nano indenter equipped with a Berkovich-tip. The load-displacement curve was analyzed according to Oliver and Pharr, where the indentation hardness, H_{IT}, is defined as the applied load divided by the projected contact area under load.[41] A constant strain rate of 0.05 s^{-1} led to a prescribed displacement of 5 µm, followed by a load holding segment prior to unloading. For optical microscopy we used a Leica DFC495 microscope.

Results

Electrochemical characterization of dealloying.—Fig. 1A compares CV scans in the setups of routes A and B on $Ag_{75}Au_{25}$ alloys. The graphs show the second out of two consecutive runs. For route A (electrolyte: 1 M $HClO_4$, RE: Ag/AgCl) we observe a first double-peak current within the region 380–860 mV, characteristic of oxygen electro-sorption onto both elements. The onset of a large anodic current, indicating Ag dissolution was found at 920 mV. The onset potential for selective Ag dissolution is consistent with findings by Pickering,[42] Sieradzki[43] and Dursun,[44] who report potentials between 890–1090 mV. The electrochemical signature in route B (electrolyte: 5 M HNO_3, RE: Pt) is similar, yet all features are shifted by ~ −1 V. We find that the dealloying potentials chosen by Parida, $E_d^A = +1050$ mV vs. Ag/AgCl,[29] and by Wittstock, $E_d^B = +60$ mV vs. Pt,[45] cause similar current densities, 25 mA/cm². These potentials were adopted for all further dealloying processes.

Attempts at repeating the CV of route B with a Ag/AgCl RE provided no reproducible results. We attribute this to a conversion of AgCl in the RE to Ag_2O under the harsh experimental conditions.

Charge transfer.—Fig. 1B depicts current density transients for dealloying at 1050 mV vs. Ag/AgCl (route A) and at 60 mV vs. Pt (route B). For route B higher current values are observed after the initiation of dealloying (after 3–4 s), followed by the approach to a stable zero current plateau after approximately 1 h. Under such small polarization potentials a zero current does not imply the corrosion process to be finalized (as outlined in the introduction) so that a conclusion on corrosion rate (i.e. the loss of Ag per time) in comparison to route A is not legitimate at this point. The net charge, Q, which is transferred at the WE was obtained by integration of the electrode current; it can be compared to the expected value, Q_F, as calculated applying Faraday's law (taking volume and composition of the sample) for complete removal of Ag from the respective sample by dissolution to Ag^+. Compared to route A, Q for route B increases significantly faster. Yet, Q for route A approaches Q_F much closer than for route B and the missing charge quantity in route A is quantitatively consistent with the residual Ag (9 at.% in Fig. 1B), whereas route B has almost complete dealloying, but nevertheless larger charge deficit.

The efficiency of charge transfer is explored by a correlation between Q and the residual Ag fraction, x_{Ag}, as shown in Fig. 1C. The figure shows x_{Ag}, as measured by EDX, versus the charge ratio Q/Q_F for samples that were dealloyed for different durations. It is remarkable that the EDX Ag fraction converges to zero as the charge from current integration converges to Q_F. This suggests that the electrode current in route A is precisely representative of the charge transfer during Ag dissolution and that there is negligible compensating cathodic current.

The different observations for routes A and B have a natural explanation in the free corrosion process that we assume to concur with the electrolytic corrosion. The free corrosion in route B is manifest by a color change of the alloy sample when immersed before the application of E_d^B for a few minutes. The sample turns yellowish, indicating Ag removal at the surface. Indeed, the missing charge of Fig. 1B suggests that roughly 18% of the total Ag amount is dissolved through the process of free corrosion. A least-squares fit through the data from $HClO_4$ corrosion provides a slope of −0.83 which enables a scarce estimation of x_{Ag} from the charge ratio Q/Q_F within a range of x_{Ag}= 0–20 at.% for route A. An accurate predictability is desirable since the Ag content is discussed to crucially affect the catalytic activity[23,46] and the mechanical properties of NPG.[47] This experimental approach to x_{Ag} has no analog in route B. This is contrary to the literature

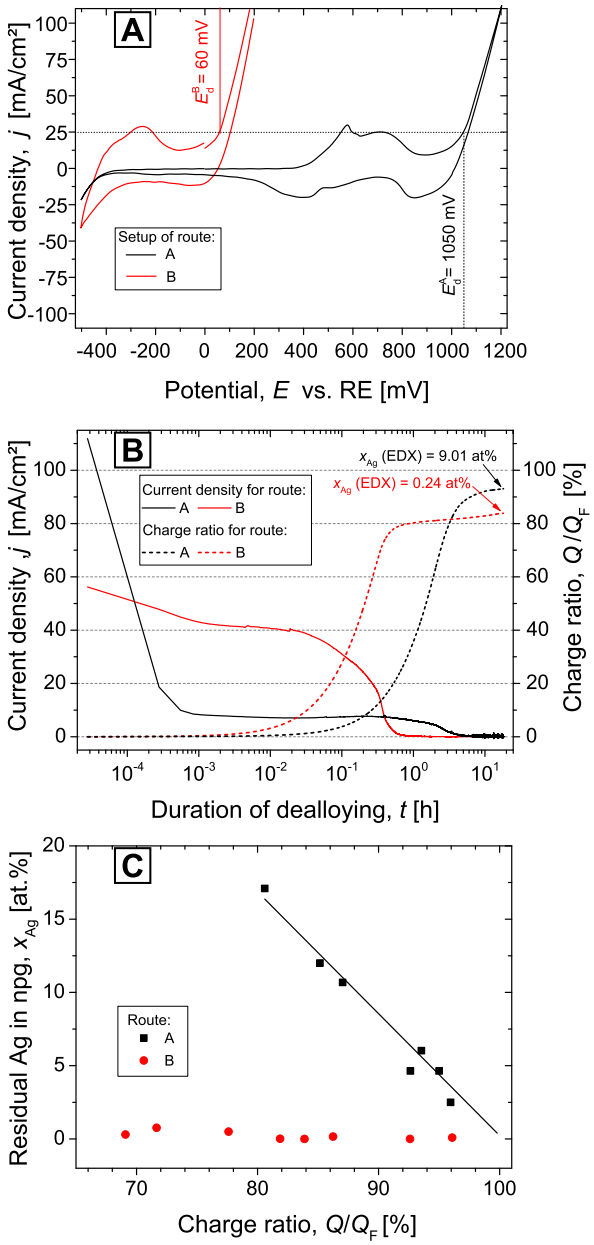

Figure 1. Comparison of process data for routes A and B: (A) Cyclic voltammograms of $Ag_{75}Au_{25}$ installed as working electrode (WE) in both dealloying setups including different reference electrodes (RE) to obtain the dealloying potentials $E_d^{A,B}$. (B) Current density (solid lines and left ordinate) and charge transients (dashed lines and right ordinate) during dealloying for both routes. Current density refers to the external surface area of the alloy sample and measured charge, Q, refers to the theoretically necessary charge, Q_F for full dissolution of 75 at.% Ag. The residual Ag content, x_{Ag}, as measured by energy-disperisve X-ray spectroscopy (EDX) refers to the measured Ag content in the dealloyed sample after 24 h. (C) Residual Ag fraction, x_{Ag}, from EDX versus the charge ratio for several samples as obtained by varying the duration of dealloying. Black straight line represents linear regression to data of route A. Black and red symbols refer to routes A and B, respectively.

where a full attribution of the measured charge to the Ag dissolution process was reported.[19,25] Besides the partial current compensation by a cathodic process in route B, an alternative explanation approach involves the ill-defined offset potential of the used Pt RE used.

Ligament size.—Figs. 2A–2C show scanning electron micrographs of samples made by routes A to C, respectively. The left column of images refers to the microstructure in the bulk, as revealed on fracture surfaces. The right column refers to the external surface of the sample. Numbers in the figures indicate the respective mean ligaments sizes.

Similar microstructures are seen to emerge from all three processes. Yet, the bulk ligament size, L_B, increases in the order route A < B < C. Fig. 2E shows the evolution of L_B during the progression of dealloying. Its increase with dealloying time is a feature that the two HNO_3-based routes have in common (as described for free corrosion by Okman and Kysar[48] or Ding et al.[49]) whereas no significant change is noticed when the dealloying is carried out in $HClO_4$.

We additionally modified route A with further steps of increased E_d^A in order to decrease x_{Ag}. The corresponding potential protocol is illustrated in Fig. 2D. No increase in ligament size upon increased potential is observed.

Surface layers.—The evolution in ligament size over time applies most obviously in the bulk, but is also reflected in the surface structures. Figs. 2A–2C illustrate that the external sample surface systematically exhibits a considerably smaller structure size than the bulk. The cross-sectional SEM image of a near-surface region, Fig. 3A, illustrates that the smaller ligaments are confined to a thin superficial layer. Smaller ligaments were found at the surface of samples made by both electrochemical processes but not in the free corrosion samples (see Fig. 2F) where the surface ligament distribution was found to be slightly broader. The ratio between L_B and L_S remains nearly unity for route C throughout the whole process. For the two electrochemical routes, coarser bulk structures evolve in different ways: Whereas there is no significant change for route A, route B starts with nearly no difference between surface and bulk, followed by a drastic increase in L_B and a decrease of L_S over time to values $L_B = 44\ nm$ and $L_S = 13\ nm$.

Averaging ligament sizes parallel to the rim (where the fracture surface meets the outer surface) at various depths provides the graph in Fig. 3B, which shows that the characteristic thickness of the surface layer is in the order of 100–150 nm.

Residual Ag.—The decrease in Ag content with dealloying time is shown in Fig. 2G. For durations up to 18 h the rate of Ag dissolution (i.e. corrosion rate) increases in the order B > A > C while in the later moments the dissolution in C is accelerated. In both HNO_3 processes more Ag is removed than in route A. Furthermore, with constant $E_d^A = 1050$ mV, route A saturates near $x_{Ag} = 9$ at.%. Further steps of increased potential reduced the Ag content from 9 at.% to 3.8 at.%.

Shrinkage.—Fig. 2H shows the time variation of the relative change in thickness, $\varepsilon = (l - l_0)/l_0$, as measured after the dealloying for series of samples with different dealloying times. As a common feature for all three routes, one observes a continuous shrinkage during the entire dealloying process. Meaningful data could only be obtained after the corrosion completely penetrated the specimens (which took at least 6 h); this motivates the absence of data points for small corrosion times in the graph.

When comparing microstructures after 24 h of dealloying, route A gives least (<3%) and route B most (8%) shrinkage, while route C is intermediate (4.3%).

Mechanical properties.—Studies of the mechanical behavior of nanoporous gold in general use L_B and φ as decisive microstructural parameters.[17,26,27,50–54] Our study finds that these parameters vary between the different synthesis routes. Indentation testing allows a rough investigation of the consequences on the mechanical behavior. We selected a comparatively large indentation depth of 5 μm to minimize the impact of surface roughness. The latter, mostly due to cold rolling of the precursor alloy, is visible as continuous notch lines in the micrographs of Figs. 4A–4C, left column. In Fig. 4B it can be seen that no crack-free areas with the size of the residual impression exist for samples manufactured by route B. For the other manufacturing routes, indents were performed on crack-free areas. Post-indent microscopy (Figs. 4A–4C right column) verified the alignment of the

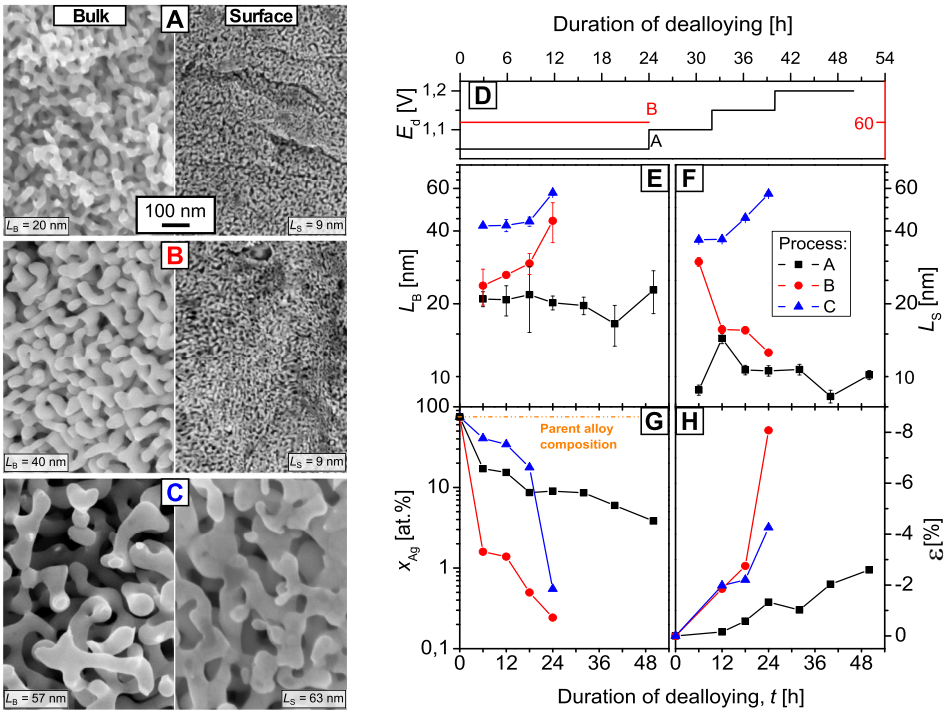

Figure 2. Microstructural features of nanoporous gold (NPG) as obtained by the three dealloying routes. (A-C) Scanning electron microscopy (SEM) images in cross-view of the bulk (left row, with bulk ligament sizes, L_B) and top-view (right row, with surface ligament sizes, L_S,) onto the surface of npg as obtained by routes A (A), B (B) and C (C). The scale bar in (A) applies to all images. (D) Applied dealloying potentials $E_d^{A,B}$ over time for route A and B, respectively (left axis: route A, right axis: route B. (E-H) Time evolution of microstructural features L_B (E, logarithmic), L_S (F, logarithmic), residual Ag content, x_{Ag} (G, logarithmic) and sample thickness shrinkage, ε (H, linear), as defined in the text. The legend in Fig. 2E applies to all graphs. Each data point in (E)-(H) corresponds to a separate sample, dealloyed for the indicated time.

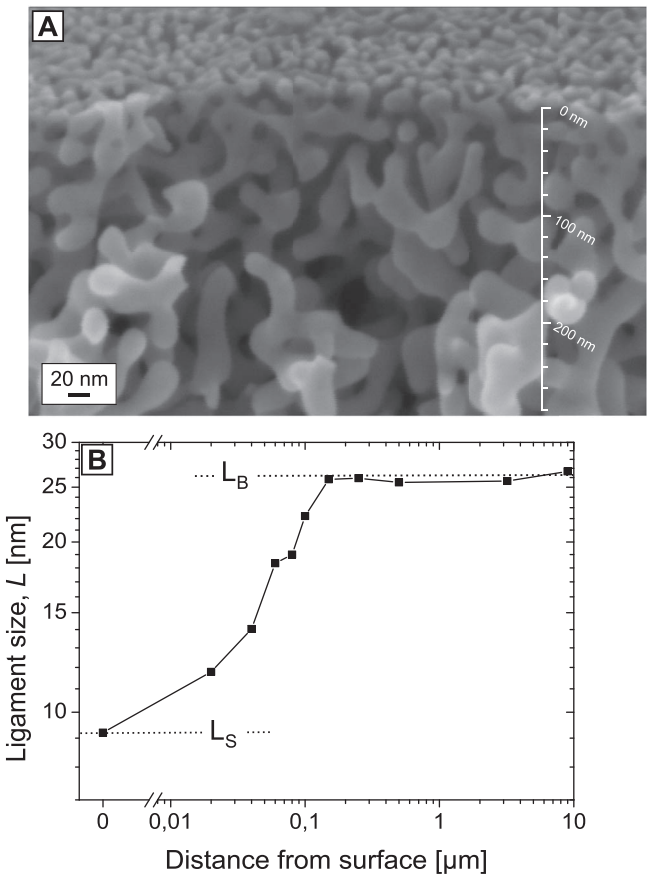

Figure 3. Comparison of ligament sizes in nanoporous gold between sample surface and bulk for NPG produced by route A. A: Scanning electron microscopy image of a cross-section of a 50 h dealloyed sample after route A with ligament sizes on surface $L_S = 9$ nm and in bulk, $L_B = 26$ nm. B: Sample depth-dependent ligament size as measured from image A.

indenter axis perpendicular to the specimen surface and the absence of newly formed cracks during the indentation process, suggesting that the material deforms in a ductile manner. Fig. 4D shows indentation hardness, H_{IT} vs. L_B for samples from the three preparation routes. Error bars represent the standard deviation in sets of several indents. The indentation hardness is roughly compatible with the well-known relation of more strength at smaller ligament size.[27,50,55–57] The shaded area represents the region between two trend lines with a slope of −1, as suggested by the experimental data from macroscopic compression tests summarized by Mameka et al.[26] This region is seen to include all data points.

Discussion

Ligament size.—The differences in ligament size, as obtained by routes A – C, are remarkable. In principle, a difference of the initial ligament or pore size in the early stage of dealloying is a conceivable origin. Yet, this hypothesis is poorly compatible with our understanding of the atomic-scale dealloying mechanism. The initial pore size is expected to reflect a competition between the removal of Ag and the nucleation of vacancy islands on crystal terraces.[58] The higher corrosion rate of route B suggests a larger nucleation rate, thus a smaller spacing between pores and generally a finer microstructure. Yet, as is illustrated in Fig. 2E, the opposite is found: The faster corrosion of route B gives larger ligaments than route A. This suggests that the different structure sizes are not representative of the initial microstructural scale at the corrosion front. Instead, we are led to assume that the different chemical or electrochemical environments provide the basis for different coarsening rates. The coarsening rate (i.e. the increase of L_B with time) scales with the surface diffusivity of gold, D_S^{Au}, since surface diffusion is regarded as the dominant mode for coarsening.[59,60] Let us summarize what is known about D_S^{Au} in different environments. A value for D_S^{Au} at the Au-$HClO_4$ interface, derived by kinetic Monte-Carlo calculation, is $2 \cdot 10^{-20}$ m^2/s.[61] Experimental data for that interface appears not available. Further it is known that adsorbed anions strongly affect D_S^{Au}.[62] Besides oxygen (which is a possible adsorbate in all routes A-C), ClO_4^- and NO_3^- are possible adsorbates. ClO_4^- anions (as present in route A) do not specifically adsorb onto the Au surface[63] and should not significantly alter D_S^{Au}. NO_3^- anions (as present in routes B-C) adsorb on Au at

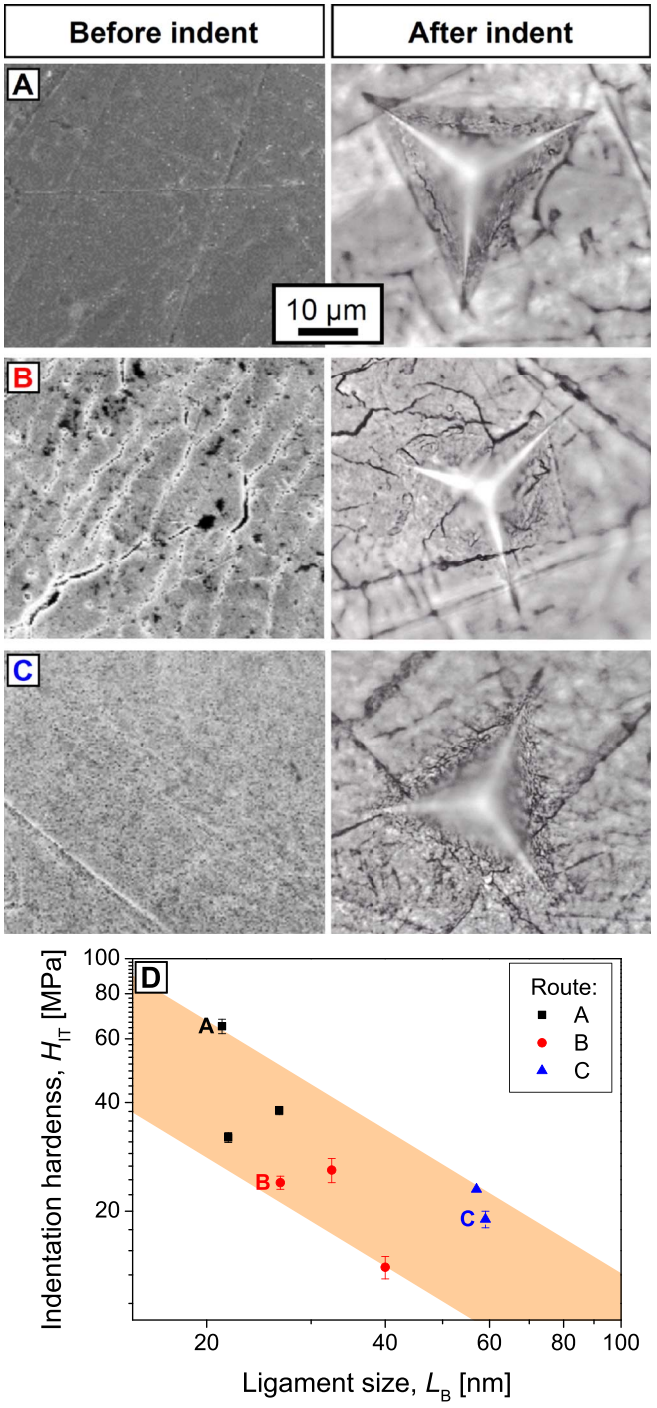

Figure 4. Impact of dealloying protocols A-C on mechanical behavior. A-C: Micrographs of indent regions for selected samples as indicated in D. Left row: scanning electron microscopy (SEM) images before indentation. Right row: optical micrographs post indentation. Scale bar in Fig. A applies for all. D: Indentation hardness, H_{IT}, versus bulk ligament size L_B.

potentials below the dealloying potential;[64] this is known to increase D_S^{Au} to $2 \cdot 10^{-19}$ m^2/s[65] leading to coarser ligaments. The presence of adsorbates was already found to influence the critical dealloying potential[59,66] so that we conclude that stronger adsorbing anions in the electrolyte finally lead to coarser ligaments because of a surface diffusivity promotion upon their adsorption.

Surface layer.—It has been reported earlier that the microstructure at the surface of dealloyed porous samples is finer and possibly denser than in the bulk.[67] This phenomenon, which is supported by our observations, may be related to differences – between bulk and surface – in the nature of sources and sinks for adatom diffusion. Systematic detachment of atoms from step edges near the surface removes terraces from there, displacing the macroscopic sample surface inward and thereby increasing φ in a thin layer at the surface. This process has no equivalent in the bulk, where dislocation climb (and, hence *lattice* diffusion) would be required to remove lattice planes. Within a continuum picture, the ligaments terminating at the surface have systematically more positive mean curvature than the interconnected ligaments in the bulk of the metal network structure. More positive mean curvature means increased chemical potential; the surface ligaments are therefore systematically sources for ad-atoms. In other words, they exhibit a comparatively larger tendency for dissolution and less for coarsening than the ligaments in the bulk. This notion is consistent with a small ligament size at the surface.

Because a significant difference of route C to route B is the increased temperature (which can cause faster coarsening of the surface), we assume this as the suspected origin for the absence of finer surface layers that were exclusively observed for samples that were dealloyed under a polarization potential $\neq 0$ (i.e. by routes A and B).

Within the notion of surface microstructure evolution as suggested above, the thickness of the surface layer scales with a characteristic diffusion length. Our observations put this range at roughly around 100 nm.

Ag retention.—The residual Ag fraction, x_{Ag}, is closely related to the mechanisms of corrosion. The removal of Ag enriches the atomic layers at the corrosion front in Au and tends to passivate the surface. As the corrosion proceeds into the depth, the passivation is bypassed through bifurcation of the pore bottom and the formation of bulk porosity. The advancing corrosion front leaves behind ligaments with Au-rich surfaces and with bulk regions that have not yet been exposed to electrolyte and that, hence, are rich in Ag. Later coarsening exposes these regions to the electrolyte, enabling further dissolution of Ag. This suggests that an increase of L_B by coarsening goes hand-in-hand with a decrease of the residual Ag content. Fig. 5 explores this correlation by plotting x_{Ag} versus L_B.

By inspection of Fig. 5 it is seen that the two electrolytic corrosion routes A and B merely differ with respect to the accessible range of L_B. By contrast, the two routes exhibit a common, consistent variation of x_{Ag} with L_B under a certain data scattering. This observation supports the scenario outlined above.

The samples resulting from route C follow a different trend, with larger ligaments and more Ag. In the light of similar values for D_S^{Au},

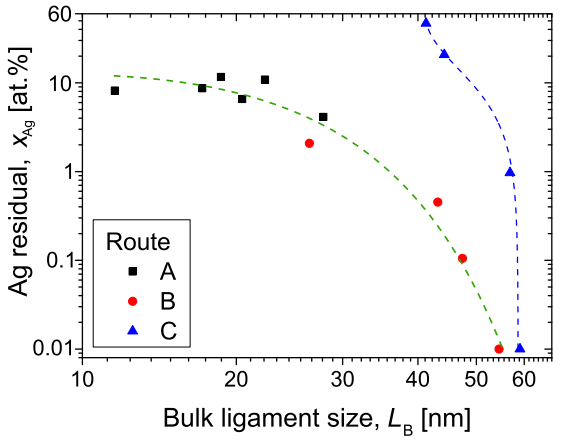

Figure 5. Correlation between the content of residual Ag, x_{Ag}, and the bulk ligament size, L_B in nanoporous gold (NPG) as dealloyed by different routes. Dashed curves represent exponential fits for NPG from electrolytic (green) and free corrosion (blue) as calculated using a least squares fit algorithm.

we speculate on different initial pore radii that are influenced by the velocity of dealloying to explain this finding.

A remarkable observation in Fig. 5 is that free corrosion – if interrupted early – may provide NPG with significantly higher Ag contents than both electrolytic corrosion procedures.

Mechanical behavior.—As stated above, the different preparation routes lead to different ligament sizes and the relation of higher hardness for smaller ligaments applies. Nevertheless, summarizing the different production routes in one graph - as done in Fig. 4D - shows deviations from the general trend. This might be related to differences in φ. It is well known that hardness and strength increase with φ.[68] Owing to their pronounced shrinkage, the route B samples would be expected to be harder. However, our results do not support this consideration. A natural explanation is provided by our observation that the shrinkage, densifying the route B samples, leads to cracking and to an extrinsic weakening. The absence of cracks and the lesser, yet still substantial, shrinkage in specimens made by route A may serve as explanation for their enhanced strength.

It has also been shown that the mechanical behavior of NPG can be drastically affected by a single monolayer of adsorbate.[69] This is significant since routes B and C create samples that are adsorption-covered by both oxygen and adsorbed NO_3^- anions while the NPG produced by route A can be assumed as oxygen-covered. It will be object of further investigations to differentiate between the specific origins of hardening/softening by different dealloying processes and surface states. Note that some of the mechanical results published in other work were obtained for NPG samples in which the oxygen adsorbate layer has been removed by electrochemical oxidation-reduction cycles.[26]

Summary

We compared three strategies for the synthesis of nanoporous gold (NPG) by corrosion of $Ag_{75}Au_{25}$, namely electrolytic corrosion under high polarization potential in $HClO_4$ (route A), electrolytic corrosion under low polarization potential in HNO_3 (route B) and purely chemical oxidation in heated semi-concentrated HNO_3 (route C). The dealloying potentials of routes A and B were found to match the values from the respective literature when selected for a current density 25 mA/cm^2 from the CVs. When the charge derived from current transients of route B is compared to the charge that is necessary to achieve the measured Ag content, we find a non-negligible deficit that might result from a compensating cathodic side reaction and prevents the direct conclusion of the residual Ag content from the measured current.

The Ag corrosion rates differ; route A has a lower rate than B. Only route A enables monitoring the residual Ag content during the corrosion progress by current integration. The NPG microstructures differ in terms of the residual Ag content (A: 3–17 at.%; B: 0–2 at.%; C: 0.5–40 at.%) and the average ligament size (A: 16–26 nm; B: 24–44 nm; C: 42–57 nm). Ligament sizes at the surface were found smaller than in the bulk for all samples of route A and for samples after extended corrosion in route B. No such effect was observed for route C. The thickness of the surface layer with smaller ligament size was found to be approximately 100 nm.

In order to explain these different features we argue for a significant impact of the chemical nature of the electrolyte on the surface diffusivity and on the kinetics of coarsening. The presence of adsorbing species was found to influence the final ligament sizes which may provide a method for their modification. By contrast, we find a strong correlation between composition and ligament size during electrochemical annealing, which is independent of the nature of the electrolyte. Samples made by electrochemical and free corrosion do not follow the same trend.

Exploring the macroscopic dimensional changes upon dealloying, we found significant differences in the shrinkage (slow and up to −3% in route A, fast and up to −8% in route B and up to −4% in route C).

Indentation tests confirm the general trend of higher hardness at smaller ligament size. The hardness data is consistent with an important impact of different solid fractions and different contents in native cracks that go along with the different preparation routes.

Nanoporous gold samples in the current literature are made by different preparation routes, three of which were explored in our work. Even though the microstructures of the samples appear quite similar upon cursory inspections, our observations establish considerable differences. Trying to explain these, it has to be noted that route A is entirely electrochemically controlled whereas route C is based on free corrosion. Route B must be regarded an intermediate case between A and C. When comparing results from studies using different preparation routes, thus care is required to verify that the microstructural characteristics and the surface states are indeed comparable.

Acknowledgments

We acknowledge Lisa Fitzek (Hamburg University of Technology) for alloy preparation, Dr. Henry Ovri & Prof. Dr. Erica Lilleodden (Helmholtz-Zentrum Geesthacht) for assistance with the nanoindentation setup and Prof. Dr. Marcus Bäumer (University of Bremen) as well as Prof. Dr. Gunther Wittstock (University of Oldenburg) for helpful discussions. This work was funded by DFG through FOR2213 "NAGOCAT".

References

1. A. Wittstock and M. Bäumer, *Acc. Chem. Res.*, **47**, 731 (2014).
2. C. Xu et al., *J. Am. Chem. Soc.*, **129**, 42 (2007).
3. J. Zhang, P. Liu, H. Ma, and Y. Ding, *J. Phys. Chem. C*, **111**, 10382 (2007).
4. E. Detsi, Z. G. Chen, W. P. Vellinga, P. R. Onck, and J. T. M. De Hosson, *J. Nanosci. Nanotechnol.*, **12**, 4951 (2012).
5. D. Kramer, R. N. Viswanath, and J. Weissmüller, *Nano Lett.*, **4**, 793 (2004).
6. C. Stenner, L. Shao, N. Mameka, and J. Weissmüller, *Adv. Funct. Mater.*, **26**, 5174 (2016).
7. F. Meng and Y. Ding, *Adv. Mater.*, **23**, 4098 (2011).
8. X. Lang, A. Hirata, T. Fujita, and M. Chen, *Nat. Nanotechnol.*, **6**, 232 (2011).
9. F. Jia, C. Yu, Z. Ai, and L. Zhang, *Chem. Mater.*, **19**, 3648 (2007).
10. Y. Xue, J. Markmann, H. Duan, J. Weissmüller, and P. Huber, *Nat. Commun.*, **5**, 4237 (2014).
11. R. Li and K. Sieradzki, *Phys. Rev. Lett.*, **68**, 1168 (1992).
12. N. A. Senior and R. C. Newman, *Nanotechnology*, **17**, 2311 (2006).
13. Y. Zhong et al., *Adv. Eng. Mater.*, **16**, 389 (2014).
14. A. Pareek et al., *J. Am. Chem. Soc.*, **133**, 18264 (2011).
15. S. Kameoka and A.-P. Tsai, *J. Mater. Chem.*, **20**, 7348 (2010).
16. X. Wang et al., *J. Phys. Chem. C*, **115**, 4456 (2011).
17. A. Mathur and J. Erlebacher, *Appl. Phys. Lett.*, **90**, 061910 (2007).
18. E. J. Gwak et al., *Scr. Mater.*, **69**, 720 (2013).
19. A. Wittstock, V. Zielasek, J. Biener, C. M. Friend, and M. Bäumer, *Science*, **327**, 319 (2010).
20. M. Hakamada and M. Mabuchi, *J. Mater. Res.*, **24**, 301 (2009).
21. J. Erlebacher and R. Seshadri, *MRS Bull.*, **34**, 561 (2009).
22. L. C. Wang et al., *Beilstein J. Nanotechnol.*, **4**, 111 (2013).
23. L. V Moskaleva et al., *Phys. Chem. Chem. Phys.*, **13**, 4529 (2011).
24. A. Wittstock, A. Wichmann, J. Biener, and M. Bäumer, *Faraday Discuss.*, **152**, 87 (2011).
25. D. Li, Y. Zhu, H. Wang, and Y. Ding, *Sci. Rep.*, **3**, 3015 (2013).
26. N. Mameka, K. Wang, J. Markmann, E. T. Lilleodden, and J. Weissmüller, *Mater. Res. Lett*, **4**, 27 (2016).
27. H. J. Jin et al., *Acta Mater.*, **57**, 2665 (2009).
28. X.-L. Ye et al., *J. Electrochem. Soc.*, **161**, 517 (2014).
29. S. Parida et al., *Phys. Rev. Lett.*, **97**, 4 (2006).
30. F. Kertis et al., *JOM*, **62**, 50 (2010).
31. J. Snyder, P. Asanithi, A. B. Dalton, and J. Erlebacher, *Adv. Mater.*, **20**, 4883 (2008).
32. H.-J. Jin et al., *Nano Lett.*, **10**, 187 (2010) http://dx.doi.org/10.1021/nl903262b.
33. L. H. Qian, X. Q. Yan, T. Fujita, A. Inoue, and M. W. Chen, *Appl. Phys. Lett.*, **90**, 9 (2007).
34. H. J. Jin, S. Parida, D. Kramer, and J. Weissmüller, *Surf. Sci.*, **602**, 3588 (2008).
35. O. Okman and J. W. Kysar, *J. Alloys Compd.*, **509**, 6374 (2011).
36. Y. Sun and T. J. Balk, *Scr. Mater.*, **58**, 727 (2008).
37. A. Y. Chen et al., *Microporous Mesoporous Mater.*, **202**, 50 (2015).
38. T. Fujita et al., *Nano Lett.*, **14**, 1172 (2014).
39. E. Rouya, S. Cattarin, M. L. Reed, R. G. Kelly, and G. Zangari, *J. Electrochem. Soc.*, **159**, K97 (2012).
40. J. Snyder, K. Livi, and J. Erlebacher, *J. Electrochem. Soc.* , **155** , C464 (2008).
41. W. C. Oliver and G. M. Pharr, *J. Mater. Res.*, **19**, 3 (2004).
42. H. W. Pickering and Y. S. Kim, *Corros. Sci.*, **22**, 621 (1982).
43. K. Sieradzki et al., *J. Electrochem. Soc.* , **149** , B370 (2002).
44. A. Dursun, D. V. Pugh, and S. G. Corcoran, *J. Electrochem. Soc.*, **152**, B65 (2005).

45. A. Wittstock, A. Wichmann, and M. Bäumer, *ACS Catal.*, **2**, 2199 (2012).
46. M. M. Montemore, R. J. Madix, and E. Kaxiras, *J. Phys. Chem. C*, **120**, 16636 (2016).
47. A. M. Hodge et al., *J. Mater. Res.*, **24**, 1600 (2009).
48. O. Okman and J. W. Kysar, in *Nanoporous Gold: From an Ancient Technology to a High-tech Material*, A. Wittstock, J. Biener, J. Erlebacher, and M. Bäumer, Editors, p. 69, Royal Society of Chemistry, Cambridge (2012).
49. Y. Ding, Y. J. Kim, and J. Erlebacher, *Adv. Mater.*, **16**, 1897 (2004).
50. A. M. Hodge et al., *Acta Mater.*, **55**, 1343 (2007).
51. J. Weissmüller, R. C. Newman, H. Jin, A. M. Hodge, and J. W. Kysar, *Mater. Res. Soc. Bull.*, **34**, 577 (2009).
52. K. Wang et al., *NPG Asia Mater.*, **7**, e187 (2015).
53. B. Roschning and N. Huber, *J. Mech. Phys. Solids*, **92**, 55 (2016).
54. N. Huber, R. N. Viswanath, N. Mameka, J. Markmann, and J. Weissmüller, *Acta Mater.*, **67**, 252 (2014).
55. A. M. Hodge and T. J. Balk, in *Nanoporous Gold: From an Ancient Technology to a High-tech Material*, A. Wittstock, J. Biener, J. Erlebacher, and M. Bäumer, Editors, p. 51, RSC Publishing (2012).
56. J. Biener et al., *Nano Lett.*, **6**, 5 (2006).
57. C. A. Volkert, E. T. Lilleodden, D. Kramer, and J. Weissmüller, *Appl. Phys. Lett.*, **89**, 87 (2006).
58. J. Snyder and J. Erlebacher, *J. Electrochem. Soc.*, **157**, C125 (2010).
59. A. Dursun, D. Pugh, and S. Corcoran, *J. Electrochem. Soc.*, **150**, B355 (2003).
60. K. Sieradzki, R. R. Corderman, K. Shukla, and R. C. Newman, *Philos. Mag. A*, **59**, 713 (1989).
61. S. A. Policastro et al., *J. Electrochem. Soc.*, **157**, C328 (2010).
62. C. Alonso, R. C. Salvarezza, J. M. Vara, and A. J. Arvia, *Electrochim. Acta*, **35**, 1331 (1990).
63. Z. Borkowska and U. Stimming, *J. Electroanal. Chem.*, **312**, 237 (1991).
64. F. Silva, M. J. Sottomayor, and A. Martins, *Electrochim. Acta*, **39**, 491 (1994).
65. L. H. Qian and M. W. Chen, *Appl. Phys. Lett.*, **91**, 89 (2007).
66. T. P. Moffat, F.-R. F. Fan, and A. J. Bard, *J. Electrochem. Soc.*, **138**, 3224 (1991).
67. S. Cattarin, D. Kramer, A. Lui, and M. M. Musiani, *J. Phys. Chem. C*, **111**, 12643 (2007).
68. L. J. Gibson and M. F. Ashby, *Cellular Solids - Structure and Properties*, 2nd ed., Cambridge University Press, Cambridge, (1999).
69. H.-J. Jin and J. Weissmüller, *Science*, **332**, 1179 (2011).